

# We are IntechOpen, the world's leading publisher of Open Access books Built by scientists, for scientists

4,800

Open access books available

122,000

International authors and editors

135M

Downloads

Our authors are among the

154

Countries delivered to

TOP 1%

most cited scientists

12.2%

Contributors from top 500 universities



WEB OF SCIENCE™

Selection of our books indexed in the Book Citation Index  
in Web of Science™ Core Collection (BKCI)

Interested in publishing with us?  
Contact [book.department@intechopen.com](mailto:book.department@intechopen.com)

Numbers displayed above are based on latest data collected.  
For more information visit [www.intechopen.com](http://www.intechopen.com)



---

# **State-of-the-Art Antenna Technology for Cloud Radio Access Networks (C-RANs)**

---

Waleed Tariq Sethi, Abdullah Alfakhri,

Muhammad Ahmad Ashraf, Amr G. Alasaad and

Saleh Alshebeili

Additional information is available at the end of the chapter

<http://dx.doi.org/10.5772/67352>

---

## **Abstract**

The cloud radio access network (C-RAN) is one of the most efficient, low-cost, and energy-efficient radio access techniques proposed as a potential candidate for the implementation of next-generation (NGN) mobile base stations (BSs). A high-performance C-RAN requires an exceptional broadband radio frequency (RF) front end that cannot be guaranteed without remarkable antenna elements. In response, we present state-of-the-art antenna elements that are potential candidates for the implementation of the C-RAN's RF front end. We present an overview of C-RAN technology and different types of planar antennas operating at the future proposed fifth-generation (5G) bands that may include the following: (i) ultra-wide band (UWB) (3–12 GHz), (ii) 28/38 GHz, and (iii) 60-GHz radio. Further, we propose different planar antennas suitable for the implementation of C-RAN systems. We design, simulate, and optimize the proposed antennas according to the desired specifications covering the required frequency bands. The key design parameters are calculated, analyzed, and discussed. In our research work, the proposed antennas are lightweight, low-cost, and easy to integrate with other microwave and millimeter-wave (MMW) circuits. We also consider different implementation strategies that can be helpful in the execution of large-scale multiple-input multiple-output (MIMO) networks.

**Keywords:** 5G antennas, 28/38 GHz antennas, 60 GHz radio, cloud computing, green RAN

## 1. Introduction

Mobile data traffic has grown 4000-fold over the past 10 years, and it is projected to grow by more than 500 times over the next few years [1]. To cope with this large demand for mobile services, the mobile communication industry is currently developing fifth-generation (5G) mobile communication systems with the objective of providing pervasive, ubiquitous, always-connected broadband data communication. Many issues must be addressed to ensure 5G networks' superior performance, such as higher energy efficiency, higher system spectral efficiency, broadened network coverage, user coverage in hot spot and crowded areas, low latency, and better quality of service (QoS). Many key enabling technologies have been suggested for 5G, including millimetric wave transmission, massive multiple-input multiple-output (MIMO) networks, small cellular cells, heterogeneous network architectures, cloud radio access networks (C-RANs), and cognitive radio [2].

Cell densification (i.e., adding more cellular cells to the network) is proposed to increase the capacity, coverage area, and spectral efficiency of 5G networks [3]. However, a major drawback of cell densification is the signal interference between adjacent base stations (BSs), which may diminish the capacity gain. Considering the issues and challenges related to the cell densification in next-generation (NGN) mobile networks, mobile operators have proposed a cost-effective and energy-efficient solution that can provide optimized performance suitable for gigabits per second (Gbps) networks: the C-RAN [2].

The architecture for a general C-RAN system is shown in **Figure 1**. In a C-RAN, the baseband units (BBUs), which consume high power, are separated from the radio access units (also called remote radio heads (RRHs)). The idea in C-RANs is to move the BBUs to a central location (data center) and connect it to the radio access units via optical fibers [4]. At a remote site, the radio access unit (RRH) consisting of the antennas and radio frequency (RF) front end performs digital processing, digital-to-analog conversion, analog-to-digital conversion, power amplification, and signal filtering [2]. Moving the BBUs to a central location improves energy efficiency, since all the baseband processing are done at the central location, called the cloud. Furthermore, the C-RAN network architecture enables inter-BS operations. Coordinated multipoint processing (CoMP) techniques can mitigate the interference between BSs and provide better management and coordination. In addition, CoMP minimizes energy consumption in MIMO systems by enabling coordinated multipoint concepts.

The performance of a 5G RAN strongly relies on an efficient RF front-end transceiver section. In addition to the amplifiers' nonlinearity, in-phase and quadrature-phase imbalance, imperfect timing causing synchronization problems, and channel interference issues, the efficiency of the RF front end is strongly affected by the antenna design, RF impairments, antennas' special dispersion causing signal distortion, mutual coupling, and broadband antennas' non-linear characteristics. Since wireless transmission involves antennas at both user terminals and the BSs, considerable attention is required in the designing and characterization of the antennas to achieve 5G networks' objectives.

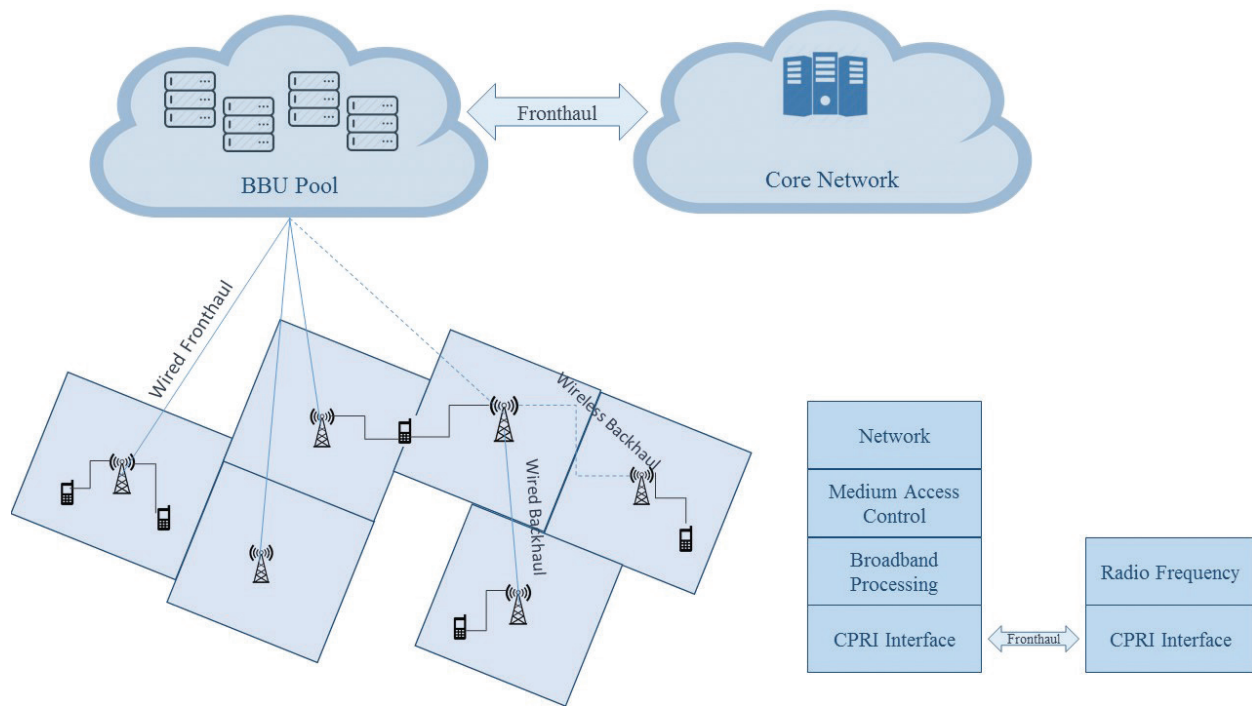


**Figure 1.** Architecture for general C-RAN system.

## 2. State-of-the-art antennas

In addition to the massive bandwidth of the antenna elements required for the implementation of NGN communication networks, several other key parameters such as gain, polarization purity, radiation efficiency, radiation patterns stability over the wide bandwidth, and minimum dispersion to the input signal are required to satisfy the systems' specifications. Antennas are classified into various types based on their key parameters/characteristics and targeted applications. In order to fulfill the ever-growing demand for wireless high-data-rate applications, ultra-wideband (UWB) technology has been considered a comprehensive solution for RF front-end design to enhance channel capacity [5]. UWB technology has drawn considerable attention, especially since the US Federal communication commission (FCC) authorized the use of the 3.1–10.6-GHz frequency band for commercial communication applications in 2002 [6]. Therefore, due to its huge bandwidth and unique feature of spectrum sharing, UWB can be considered one of the leading technologies for the implementation of NGN radio access networks, including the C-RAN.

Recent UWB antenna designs have focused on low cost, small size, and low-profile planar technology because of their ease of fabrication and their ability to be integrated with other components. The planar circuit development technique has brought monopole antennas with different shapes (polygonal, rectangular, triangular, square, trapezoidal, pentagonal, and hexagonal), circular, elliptical, etc.), which have been proposed as suitable candidates for UWB antenna systems [7, 8]. Mainly, the printed antennas consist of the planar radiator and ground

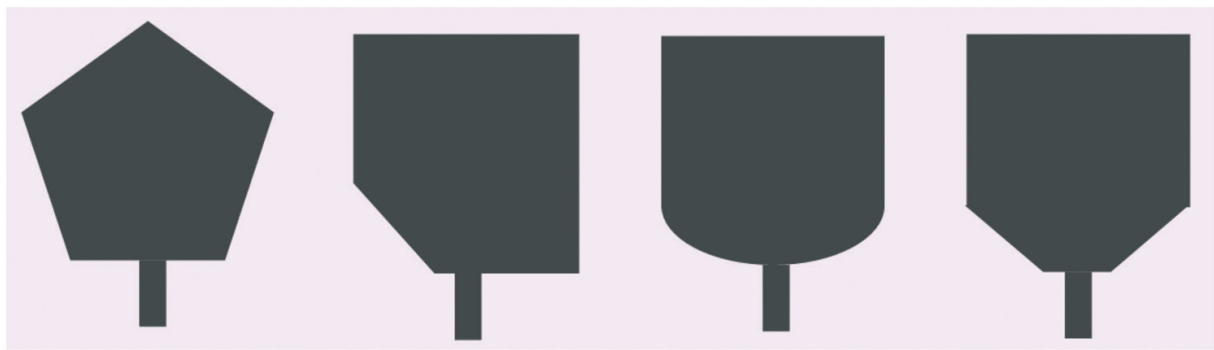
plane etched oppositely onto the dielectric substrate of the printed circuit boards (PCBs). In some configurations, the ground plane may be coplanar with the radiator. The radiators can also be fed by a microstrip line or coaxial cable [9].

Numerous microstrip UWB antenna designs have been proposed [10–15]. For instance, a patch antenna has been designed as a rectangular radiator with two steps, a single slot on the patch, and a partial ground plane etched on the opposite side of the dielectric substrate. It provides a bandwidth of 3.2–12 GHz and a quasi-omni-directional radiation pattern [10]. Moreover, a clover-shaped microstrip patch antenna has been designed with a partial ground plane and a coaxial probe feed. The measured bandwidth of the antenna is 8.25 GHz with a gain of 3.20–4.00 dBi. In addition, it provides a stable radiation pattern over the entire operational bandwidth [11]. Another design is a printed circular disc monopole antenna fed by a microstrip line. The matching impedance bandwidth is from 2.78 to 9.78 GHz with an omni-directional radiation pattern, and it is suitable for integration with PCBs [12]. In addition, several elliptical shaped-based antennas have been designed. For example, three printed antennas have been designed starting from the elliptical shape, namely the elliptical patch antenna, its crescent-shaped variant, and the semielliptical patch [13].

Another type of printed antenna is the UWB-printed antenna fed by a coplanar waveguide (CPW). For example, one trapezoidal design and its modified form cover the entire UWB band (3.1–10.6 GHz) and have a notch for the IEEE 802.11a frequency band (5.15–5.825 GHz). The frequency notch function is obtained by inserting different slot shapes into the antenna. The notch frequency can be adjusted by varying the slot's length. The antennas show good radiation patterns as well as good gain flatness except in the IEEE 802.11a frequency band [14]. Another kind of radiating element considered suitable for phased arrays is the class of Vivaldi antennas, also known as quasi-end-fire nonresonant radiator or tapered slot antennas (TSAs) [15]. However, the element is normally fabricated by cutting a notch in a metal plate and backed by a quarter-wave cavity behind the feed point to improve its forward gain. A few examples of designed and fabricated UWB monopole and directional antennas are shown in **Figure 2**.

The next generation of ongoing wireless revolution with the growing demand of wireless facilities in mobiles, the millimeter-wave (MMW) frequency band appears to be a strong candidate for future radio access technologies. In addition to UWB, MMW technology (30–300 GHz) allows the developing of miniaturized and compact antenna sensors to be used in the RF front end, thus reducing the overall size of the system [16–19]. Compared to lower frequency signals, MMW signals can propagate over shorter distances due to their larger attenuation. Therefore, the development of MMW antennas with high gain performance for wireless access networks has attracted the interest of many researchers. In order to improve the spectral efficiency and exploit the benefits of spatial multiplexing, MMW antennas are expected to be used for large-scale MIMO (i.e., massive MIMO) systems. Therefore, it is important that improving a single parameter of an individual antenna will significantly improve the overall performance of a MIMO system, since each branch of the MIMO system will find at least one of them. The following are some well-known architectures and packaging techniques for improving the performance of MMW radios in terms of bandwidth, gain, and directivity.

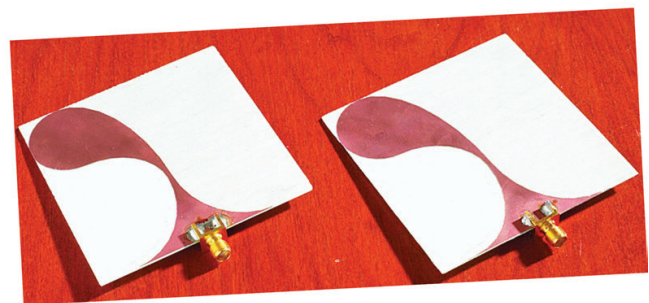
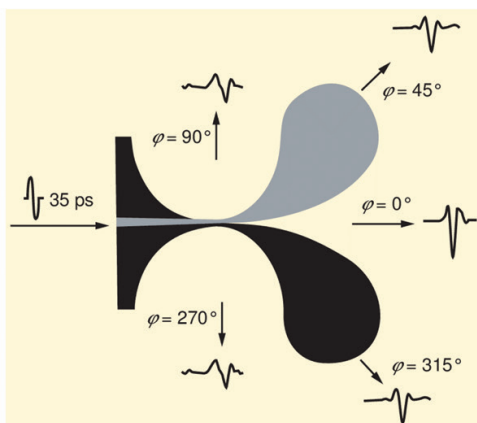




(a)



(b)



(c)



(d)

**Figure 2.** Different types of UWB antennas (a) conical antennas, (b) planar monopoles, (c) planar monopoles with band stop filters, (d) Vivaldi antennas and (e) spiral antennas [9].

Vettikalladi et al. [20] explained the significance of the addition of a superstrate on an aperture-coupled antenna at MMW frequencies. It can be seen that with the addition of a superstrate, the bandwidth is noted to be  $BW = 58.7\text{--}62.7$  GHz (i.e., 6.7%) with a maximum gain of 14.9 dBi. A new dual-polarized horn antenna fed by a microstrip patch operating in the Ku band was proposed in Ref. [21]. The patch and horn were designed separately and then assembled together. The horn antenna had a reflection coefficient of less than  $-10$  dB and a port isolation greater than 30 dB over 14.6–15.2 GHz and a gain of 12.34 dBi and 10-dB beamwidths of  $87^\circ$  and  $88^\circ$  at 14.9 GHz. The final structure had a gain of 12.34 dBi. The authors in Ref. [22] presented a wideband transition from CPW to horn antenna (CPWHA) based on the slot-coupled stacked-patch antenna technique, while those in Ref. [23] presented a wideband high-efficiency 60-GHz aperture superstrate antenna. It is found by measurement that by using a superstrate above the aperture antenna, we can improve the gain up to 13.1 dBi with a wide bandwidth of 15% and an estimated efficiency of 79%. This good result is higher than that of a classical  $2 \times 2$  array, on an RT Duroid substrate, with a gain of 12 dBi and an efficiency of 60%. In Ref. [24], a new concept of a directive planar waveguide (WG) antenna array for the next generation of point-to-point E-band communication was presented. The proposed antenna consisted of two major parts: first, the array of Gaussian horn radiating elements, and second, the mixed feeding rectangular WG network. A high-gain slot-coupled circular patch antenna with a surface-mounted conical horn for MMW applications at 31 GHz was proposed in Ref. [25]. The design adopted microstrip/conical horn hybrid technology for a 6-dB enhancement over the conventional circular patch antenna. A novel micromachining approach for realizing 60-GHz foam aperture-coupled antennas was presented in Ref. [26]. The foam is indeed an ideal antenna substrate, as its electrical properties are close to those of the air. High-gain compact stacked multilayered Yagi designs were proposed and demonstrated in the V-band in Ref. [27]. This novel design showed for the first time an antenna array of Yagi elements in an MMW-stacked structure. The measured Yagi antenna attained an 11-dBi gain over a 4.2% bandwidth with a size of  $6.5 \times 6.5 \times 3.4$  mm<sup>3</sup>. Efficient and high-gain aperture-coupled patch antenna arrays with superstrates at 60 GHz were studied and presented in Ref. [28]. The maximum measured gain of a  $2 \times 2$  superstrate antenna array was 16 dBi with an efficiency of 63%, 4 dB higher than that of a classical  $2 \times 2$  array at 60 GHz.

In order to meet recent requirements of designing large-scale MIMO wireless communication systems, conformal antenna technology enables the development of compact antenna arrays [29, 30]. Moreover, to create high-capacity MMW-MIMO systems, conformal antenna structures can be integrated with modern beam-switching technology, resulting in a data rate of several gigabytes. In cases in which the line-of-sight link is blocked, beam-switching technology allows the dynamic control of the antenna's main beam in order to find the received signal with the highest power. Several antenna arrays with beam-steering and beam-switching capabilities have been developed in Refs. [16, 31, 32]. Recently, a beam-switching conformal antenna array system operating at the 60-GHz mm-wave frequency band offering 1.5-GHz bandwidth was reported in Ref. [33]. However, the size of the developed switched beam array system was  $31 \times 46.4$  mm<sup>2</sup> rounded around a cylinder with a radius of 25 mm. Second, the simulations resulted in a gain value of 16.6 dBi.

### 3. Design of planar antennas for C-RANs

Among various devices, C-RANs have a good number of highly efficient antennas integrated with their RF front ends. In order to make these antennas more adaptable and fulfill the telecom vendors' requirements, they are expected to operate in one of the future proposed 5G bands: (i) UWB (3–12 GHz), (ii) 28/38 GHz, or (iii) 57–64 GHz suggested for system design and implementation. In this work, we will design, model, and optimize state-of-the-art antenna elements operating over the proposed frequency bands that can be considered suitable candidates for the implementation of a C-RAN's RF front end. The proposed antennas are designed to be efficient, moderate in size, low-profile (i.e., can be implemented using conventional fabrication processes), and cost-effective. In addition, the designed antennas' key parameters such as reflection coefficient, gain, radiation pattern, dispersion effect, radiation efficiency, and pattern stability are calculated and optimized to achieve the C-RAN's high data rate requirements. The following are the design details of our proposed antenna elements suggested for the implementation of the C-RAN's front end.

### 4. UWB antenna element

In this section, we present antipodal tapered slot antennas (ATSAs) with elliptical strips termination modified with elliptical-shaped edge corrugations. The proposed corrugated antenna uses elliptical slots loading to improve the gain by up to 1.9 dB over an operational bandwidth of 0.8–12 GHz. It also improves the front-to-back lobe ratio. The designed ATSA exhibits minimum distortion to ultra-short pulses of 50 ps covering the 3–12-GHz frequency band.

#### 4.1. Antenna design

The antenna element shown in **Figure 3(a)** is a traveling wave ATSA developed on Rogers 5880 substrate having dielectric constant  $\epsilon_r = 2.2$  and thickness  $h = 1.574$  mm. The size of each antenna is  $160 \times 120$  mm<sup>2</sup>.

The ATSA-EC contains strip conductors on both sides of the substrate. In order to have impedance matching over a bandwidth of more than 10:1, the tapered slot is designed by following the guidelines in Ref. [35]. The exponential taper  $C_g$  is used for the ground in order to achieve the broadband microstrip to parallel plate transition. The tapered curve  $C_g$  is defined as

$$C_g = W_y - 1 + 0.1 W_y e^{\alpha W_x} \quad (1)$$

where  $\alpha$  is the rate of transition for the exponential curve defined as follows:

$$\alpha = \frac{1}{1.92 W_x} \ln \left( \frac{W_y + 0.1 W_t}{0.1 W_t} \right) \quad (2)$$

where  $w_x$  is the  $x$ -directed length of the curve with  $w_y$  and  $w_t$  being the  $y$ -directed initial and final points, respectively. The variation of impedance bandwidth and radiation characteristics



against different geometrical parameters of proposed ATSAs are analyzed by full-wave simulation software CST Microwave Studio [36]. **Table 1** presents the geometry of the ATSA, which results in 182% impedance bandwidth with the required radiation performance.

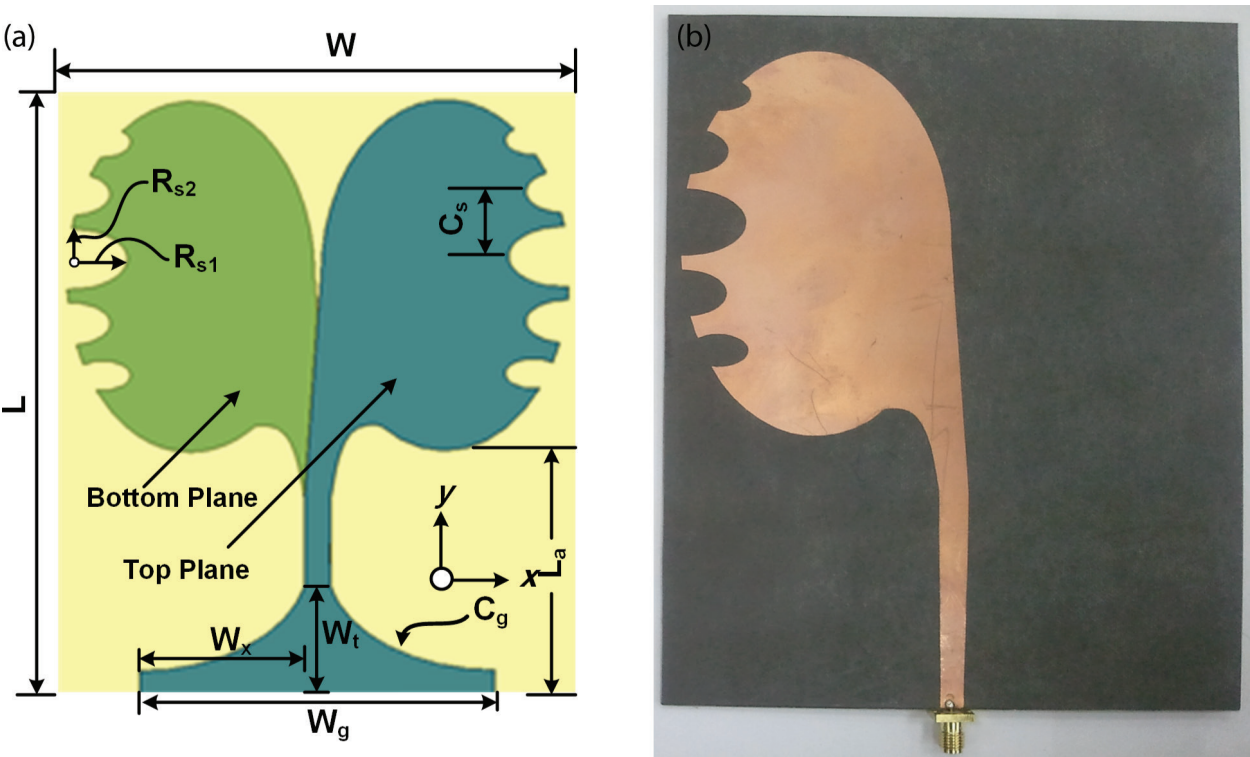


**Figure 3.** Layout diagram of (a) antipodal tapered slot antenna with elliptical-shaped edge corrugation (ATSA-EC) and (b) photograph of fabricated antenna [34].

$R_1$	$R_2$	$D$	$w_y$	$w_x$	$w_t$	$w_o$	$w_1$
32.5	42.25	65	8	43.85	35	5.95	6.12

**Table 1.** Optimized geometrical dimensions (mm) of ATSA.

In order to improve the radiation characteristics, elliptical edge corrugations are applied to the ATSA, as shown in **Figure 3(a)**. At each edge of the antenna, unequal half-elliptical slots (UHESs) are loaded with the period  $C_s = 17$  mm. The largest UHES having minor axis and major axis radii  $R_{s1} = 15$  mm and  $R_{s2} = 8$  mm, respectively, is placed at the center of the elliptical fin. Conversely, the major axis radii of the other UHESs are decreased linearly by the factor  $C_r = 0.7$  having the constant ellipticity ratio  $e_r = 0.533 = R_{s2}/R_{s1}$ .

4.2. Results and discussion

The photograph of the fabricated ATSAs is shown in **Figure 3(b)**. The measured return loss of the fabricated ATSA-EC is compared with the simulation results, as shown in **Figure 4**.

The simulation results are in good agreement with the measured performance. Generally, the radiation of an ATSA is a function of length, aperture width, and substrate thickness. The added inductance due to edge corrugation increases the electrical length of the antennas. The loading of the ATSA with UHES can suppress the surface current at both back edges, resulting in improved gain performance compared to un-slotted antenna gain. Similarly, the UHESs increase the effective length of the antenna, resulting in more directive beams in both the E- and H-planes. **Figure 5** presents the simulation results of the ATSAs' gain performance against various corrugation depths compared with un-corrugated ATSAs. The realized gain of the ATSA is found between 3 and 8.5 dBi over the 0.8–6 GHz frequency band. The edge corrugation arranges the current path to be parallel with the desired radiating current and opposite to the undesired surface current. The former enhances the gain, whereas the latter decreases the backward radiation. Therefore, the realized gain of the ATSA-EC is improved over the 0.8–6 GHz band by varying elliptical slots radii  $R_{s1}$  and  $R_{s2}$ . Comparatively, better gain improvement is found for the ellipticity ratio  $e_r = R_{s2}/R_{s1}$  less than 0.35, as depicted in **Figure 5**.

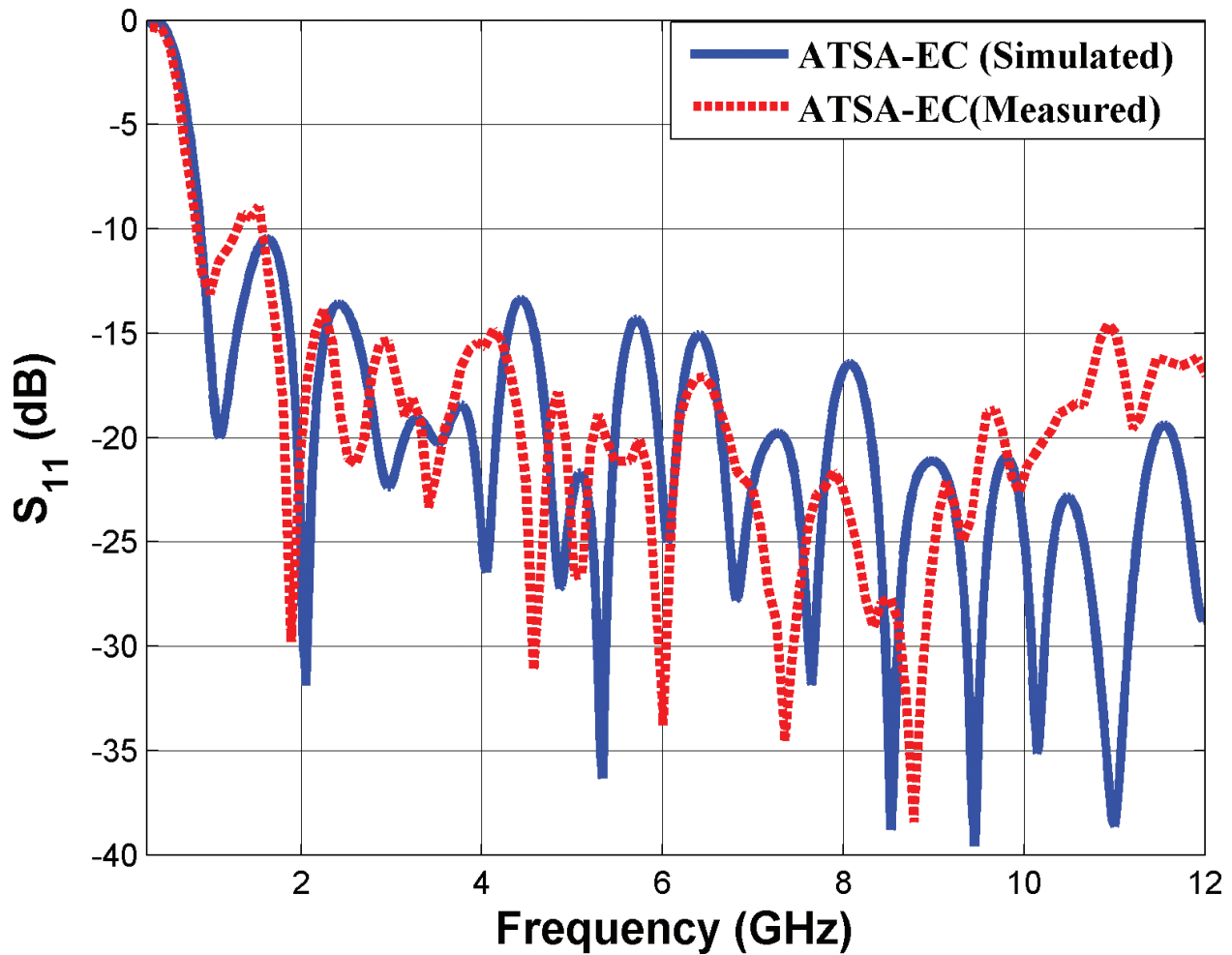


**Figure 4.** Measured return loss characteristics of fabricated ATSA-EC [34].

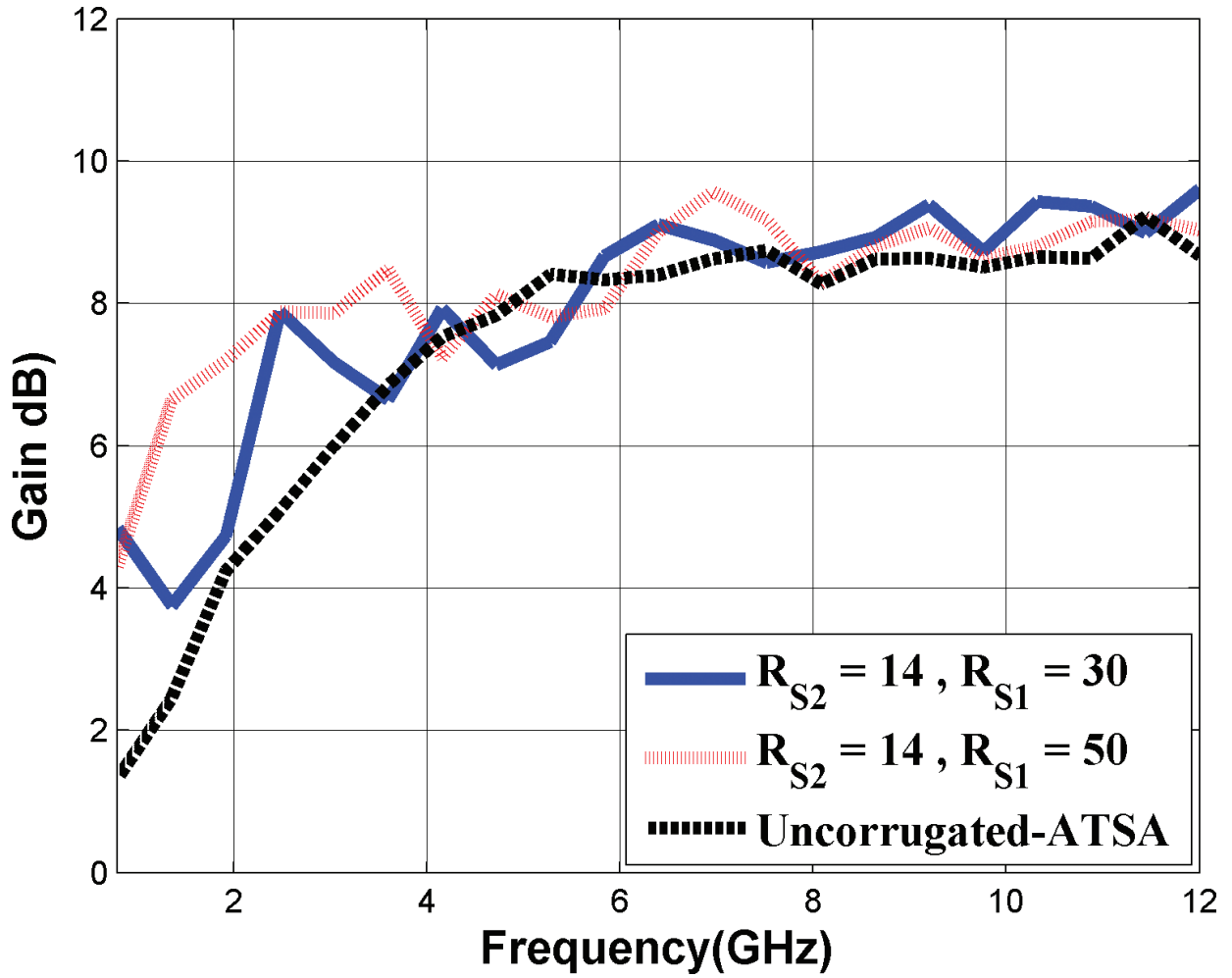
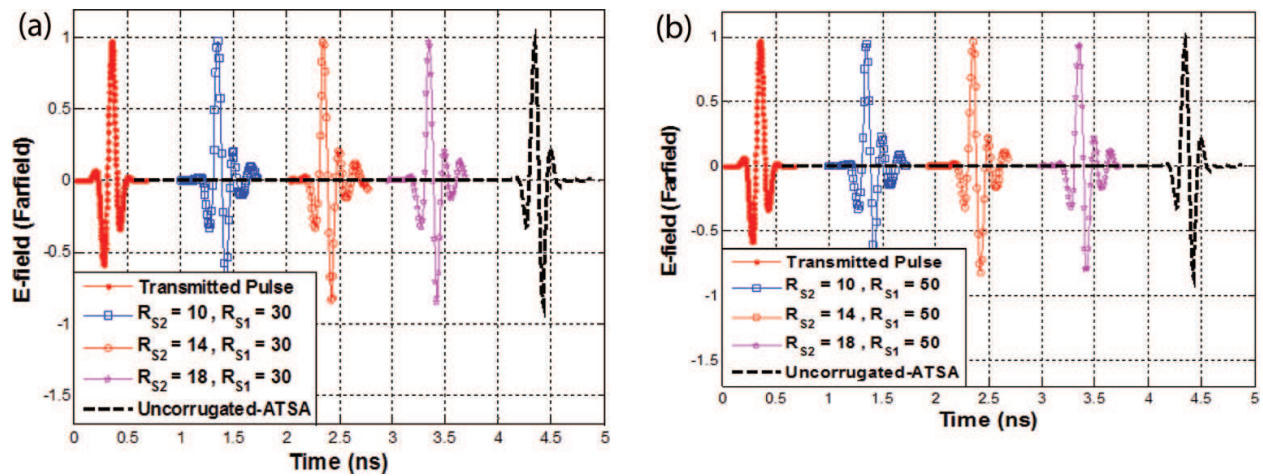


Figure 5. Simulated gain characteristics of ATSAs at different edge corrugation values [34].

The simulated time domain response of ATSAs when excited with pass-band Gaussian pulses covering the complete spectrum of operating frequency is shown in **Figure 6**. The received pulses are obtained by placing an  $x$ -oriented  $E$ -field probe 10 m along the broadside direction of the antenna. The FWHM of the transmitted pulse is 50 ps, while the received pulses preserve the Gaussian shape having a maximum FWHM of 56 ps related to the ATSA-EC with  $R_{S1} = 30$  mm and  $R_{S2} = 18$  mm. The FWHM of the ATSA without corrugation and ATSA-EC with  $R_{S1} = 50$  and  $R_{S2} = 14$  are found to be 58 and 59 ps, respectively. The fidelity factor is calculated according to the following relation [37].

$$Fidelity = \max_t \frac{\int_{-\infty}^{\infty} S_t(t) S_r(t-\tau) dt}{\sqrt{\int_{-\infty}^{\infty} |S_t(t)|^2 dt \int_{-\infty}^{\infty} |S_r(t-\tau)|^2 dt}}, \quad (3)$$

where  $S_t(t)$  and  $S_r(t)$  represent the transmitted and received time domain pulses, respectively. The fidelity factors for ATSA-EC at different edge corrugations are presented in **Table 2**.



**Figure 6.** Simulated transmitted and received pulses on E-field probe for different edge corrugation parameters [34].

$R_{s2}$	10	14	18	10	14	18
$R_{s1}$	30	30	30	50	50	50
Fidelity	0.89	0.88	0.87	0.91	0.92	0.9

**Table 2.** Calculated fidelity factor for ATSA-EC at different edge corrugation.

## 5. Compact switched-beam MMW conformal antenna array system

This section presents a conformal ATSA system designed for future 5G wireless communications. A compact ( $25 \times 30$ -mm<sup>2</sup>) ATSA element is designed presenting the reflection coefficient value less than  $-10$  dB over a wide spectrum covering the 14.8–40-GHz frequency band. The MIMO antenna system is comprised of four ATSAs. Antenna elements are placed  $90^\circ$  apart from each other over a small cylinder having a 12-mm radius. The conformal ATSAs are loaded with a dielectric lens for gain enhancement. The optimized dimensions of the dielectric lens are obtained by several full-wave simulations resulting in a gain value of more than 20 dBi from 24 to 40 GHz. The proposed system presents four orthogonal independent beams switched at the angle of  $\pm 14^\circ$  along the coordinate axis.

### 5.1. Broadband MMW ATSA design

The geometry of the ATSA antenna is shown in **Figure 7(a)**. The antenna was designed on RT/duroid® 5880 laminate having a dielectric constant of  $\epsilon_r = 2.2$  and a thickness of 0.254 mm. The top and the bottom plane conductors form an antipodal feed arrangement, enabling the ATSA antenna to exhibit excellent broadband characteristics. The tapered ground plane is obtained by cutting a half-ellipse with the radii of the major axis and minor axis,  $r_1$  and  $r_2$ , respectively.

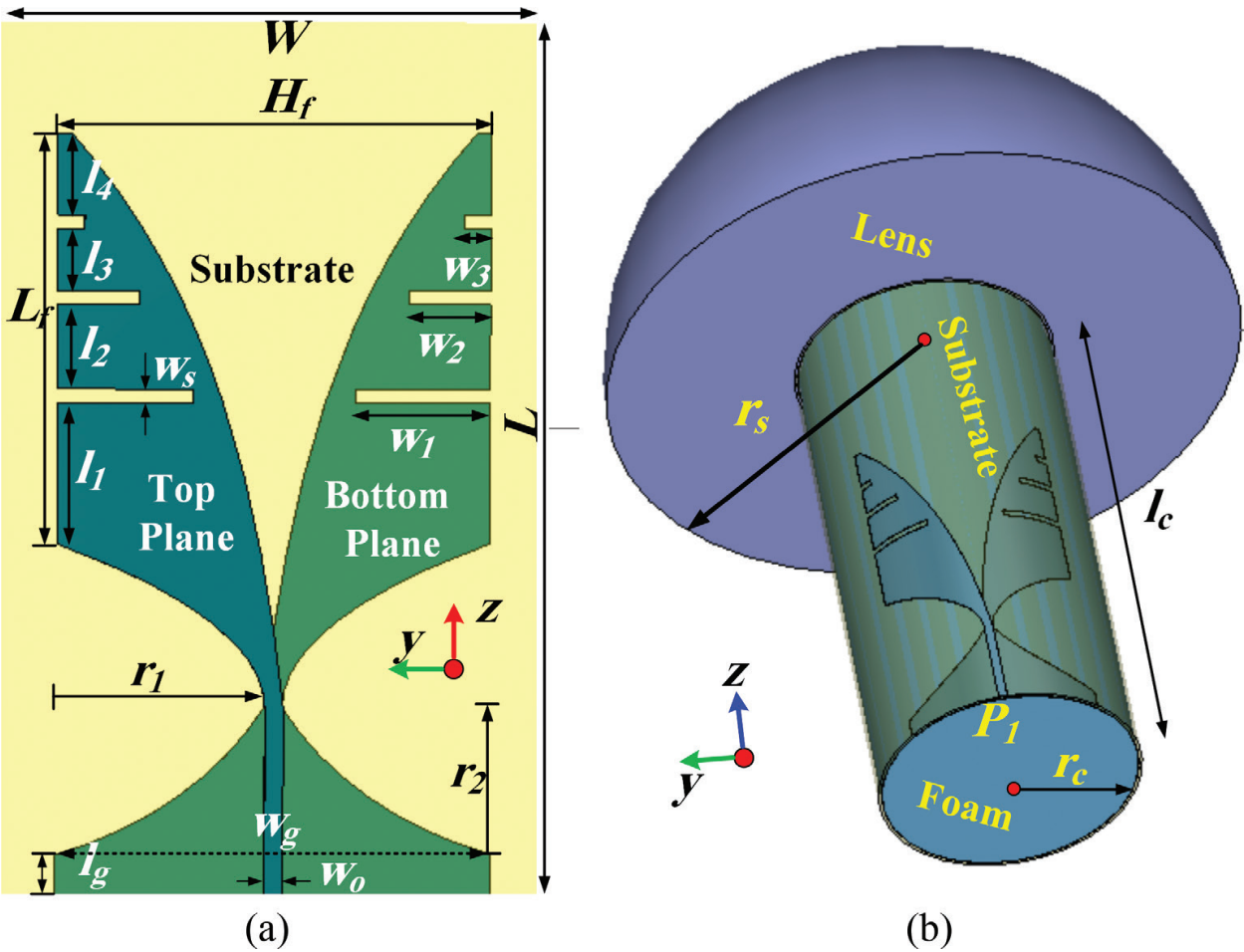


Figure 7. Geometry of ATSA, (a) rectangular configuration, (b) lens-loaded conformal configuration [38].

The top plane and the bottom plane conductors are tapered according to the guideline given in Ref. [17]. In order to reduce backward radiations, the linear corrugation is designed and optimized by executing several full-wave simulations using the CST Microwave Studio computer program. The optimized parameters of the ATSA are listed in Table 3.

Parameter	$W$	$L$	$H_f$	$L_f$	$l_g$	$W_0$	$W_g$	$r_1$
Value (mm)	24	32	16	15	1.63	0.67	16	7.6
Parameter	$l_1$	$l_2$	$l_3$	$l_4$	$w_1$	$w_2$	$w_s$	$r_2$
Value (mm)	5.15	3.07	2.27	2.99	5	3	0.5	5.36

Table 3. Optimized dimensional parameters of the proposed antenna.

The geometry of the proposed conformal ATSA is shown in Figure 7(b). The ATSA element is designed over a low-thickness flexible substrate, which allows us to round the antenna



element over a cylindrical surface. We selected a cylinder of foam material to preserve the electrical characteristics of the designed antenna. The radius of the foam cylinder is 12 mm. In order to enhance the gain, the ATSA is loaded with a half-spherical dielectric lens with a relative permittivity of  $\epsilon_r = 2.2$  and optimized radius ( $r_s$ ) of 32 mm. The length ( $l_c$ ) of the conformal structure is the same as that of the nonconformal antenna, which is equal to 32 mm. The calculated performance parameters of the proposed antenna structures are discussed in the following subsections.

## 5.2. Results and discussion

The ATSA of the conventional rectangular shape was first optimized to exhibit a  $-10$  dB bandwidth over a wider frequency spectrum. In the conformal antenna design, the radius of the foam cylinder is optimized for a minimum realizable value without compromising the electrical performance of the original ATSA. Finally, a dielectric lens is introduced toward the end-fire direction of the conformal ATSA, and S-parameter values are calculated. The S-parameter curves of the ATSAs having rectangular, conformal, and lens-loaded conformal configurations are presented in **Figure 8**, showing  $S_{11}$  values less than  $-10$  dB from the 14.8 to 40-GHz frequency band. All three curves presenting the reflection coefficient performance of different ATSA configurations are found to be in close agreement with each other. The rectangular-shaped ATSA radiates toward the end-fire direction with E- and H-plane pattern symmetry. **Figure 9(a)** and **(b)** compare the normalized radiation patterns of ATSAs' rectangular, conformal, and lens-loaded configurations at 28 and 38 GHz, respectively. The conformal ATSA without a lens exhibits almost the same radiation pattern as the rectangular ATSA at both frequencies, except there is a shift of  $4^\circ$  in the H-plane pattern. The ATSA configurations

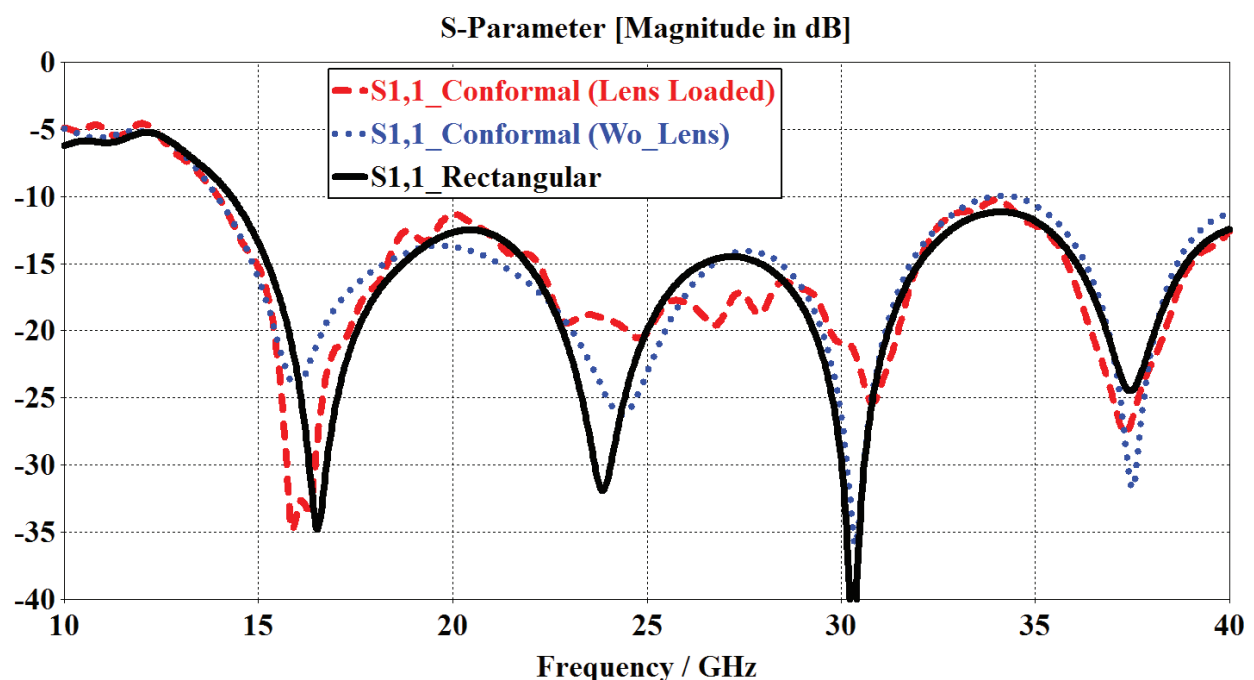


**Figure 8.** Reflection coefficient versus frequency of three different configurations of proposed ATSA [38].

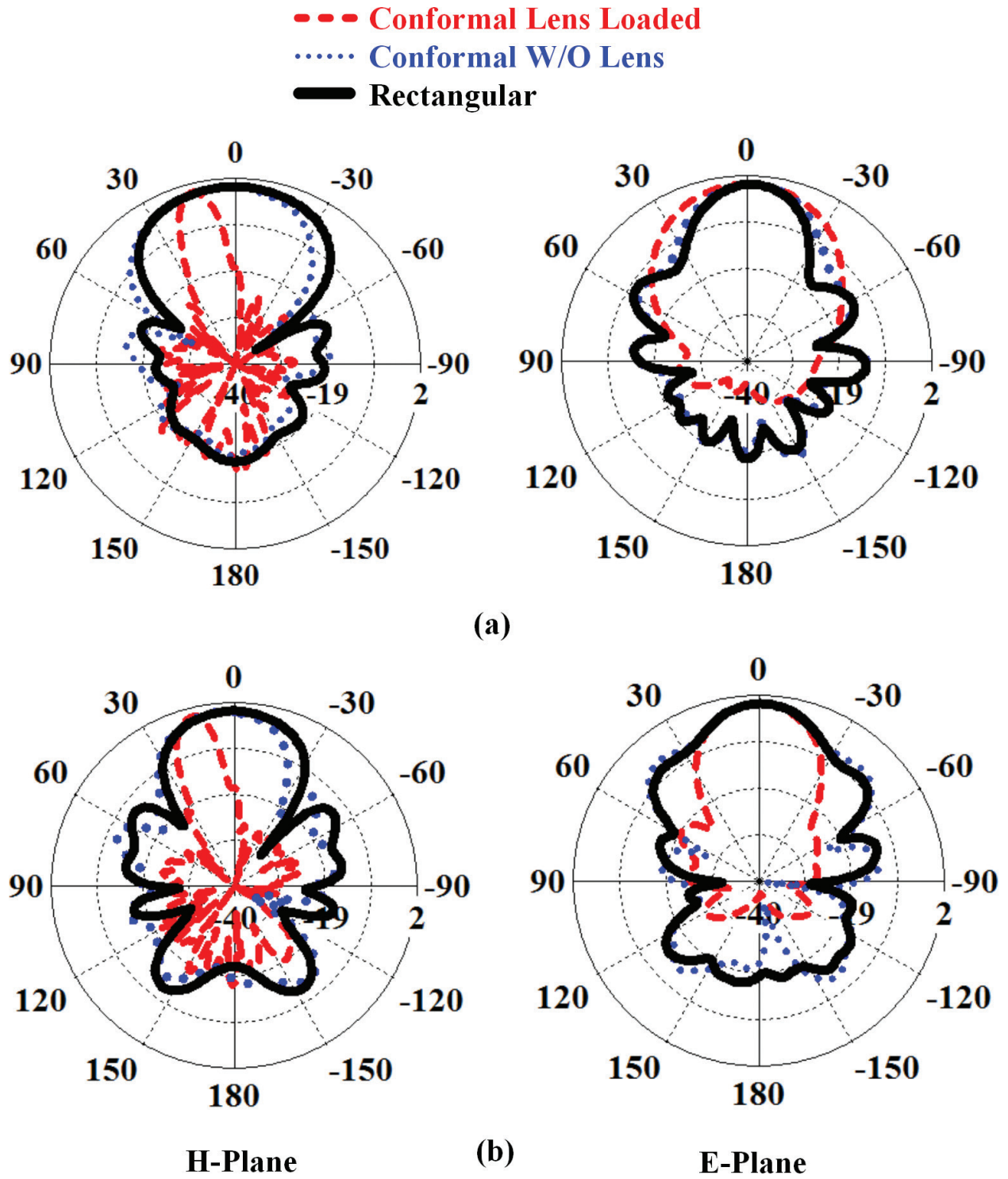


**Figure 9.** Copolarization radiation patterns in  $\phi=0^\circ$  (H-plane) and  $\phi=90^\circ$  (E-plane) cuts at (a) 28 GHz and (b) 38 GHz [38].

without a lens present an average 3-dB beam-width of more than  $40^\circ$  in both planes. On the other hand, the lens-loaded ATSA finds a  $14^\circ$  shift in the H-plane beam with a 3-dB angular width of  $12^\circ$ . The introduction of the dielectric lens toward the end-fire direction enhances the gain of a conformal ATSA due to the focusing of the radiated field in space. The diameter

of the dielectric lens is optimized by several full-wave simulations. The results presenting a parametric study of gain versus frequency against different diameters of dielectric lens are shown in **Figure 10**. A significant improvement (i.e., more than 10 dB) in gain parameters is observed by increasing the radius ( $r_s$ ) of the dielectric lens up to 32 mm. **Table 4** presents the comparison of the radiation characteristics among the three configurations of the ATSA .

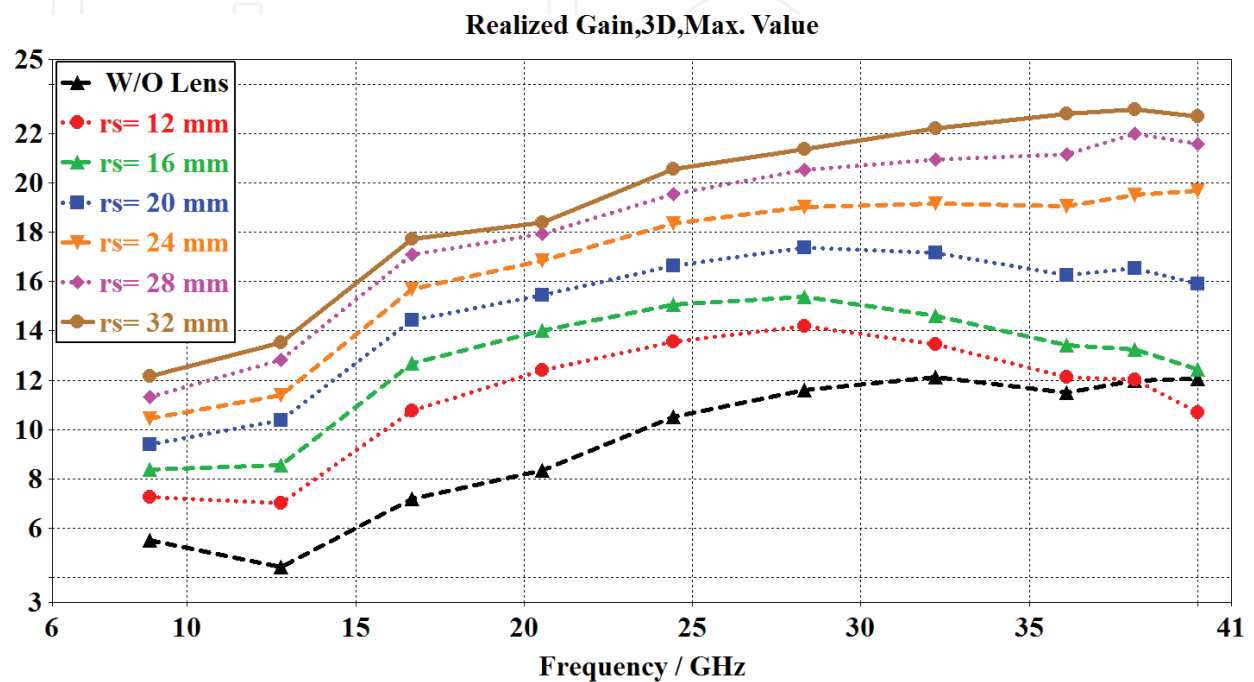


**Figure 10.** Gain versus frequency against different radii of dielectric lens loaded toward end-fire direction of ATSA [38].

	Peak gain (dBi)	Radiation efficiency (%)
Element 1	6.06	97
Element 2	5.18	98
Element 3	5.50	97

**Table 4.** Comparison of peak gain and radiation efficiency among the MIMO antenna systems.

### 5.3. Four-element beam-switched MIMO ATSA system

The geometry of the proposed conformal MIMO antenna system is shown in **Figure 11**. The four ATSA elements are placed along the  $\pm x$ ,  $y$  co-ordinate axis of a 12-mm-radius cylinder. The physical separation between the subsequent antenna elements is  $d_c = 17$  mm, which is  $1.58 \lambda_0$  at 28 GHz. The dimensions of conformal MIMO ATSAs are the same as mentioned previously. Antenna elements 1 and 2 are approximately perpendicular to each other, placed parallel to the  $yz$ -plane and  $xz$ -plane, respectively. Similarly, antenna elements 3 and 4 are placed opposite to antenna elements 1 and 2, respectively.

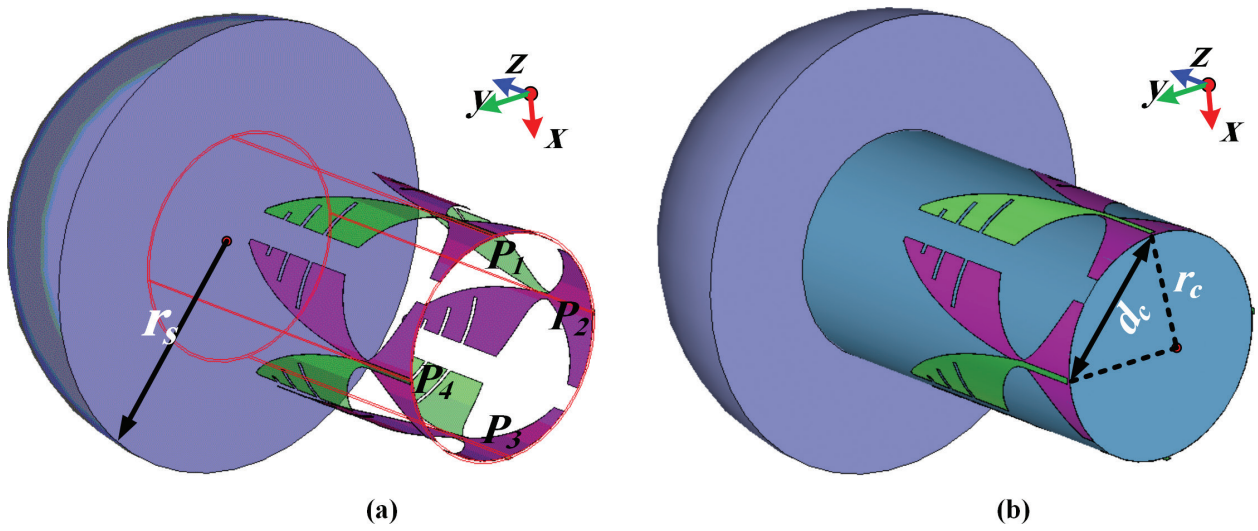


**Figure 11.** Geometry of four-element switched-beam MIMO antenna system, (a) transparent view and (b) solid view [38].

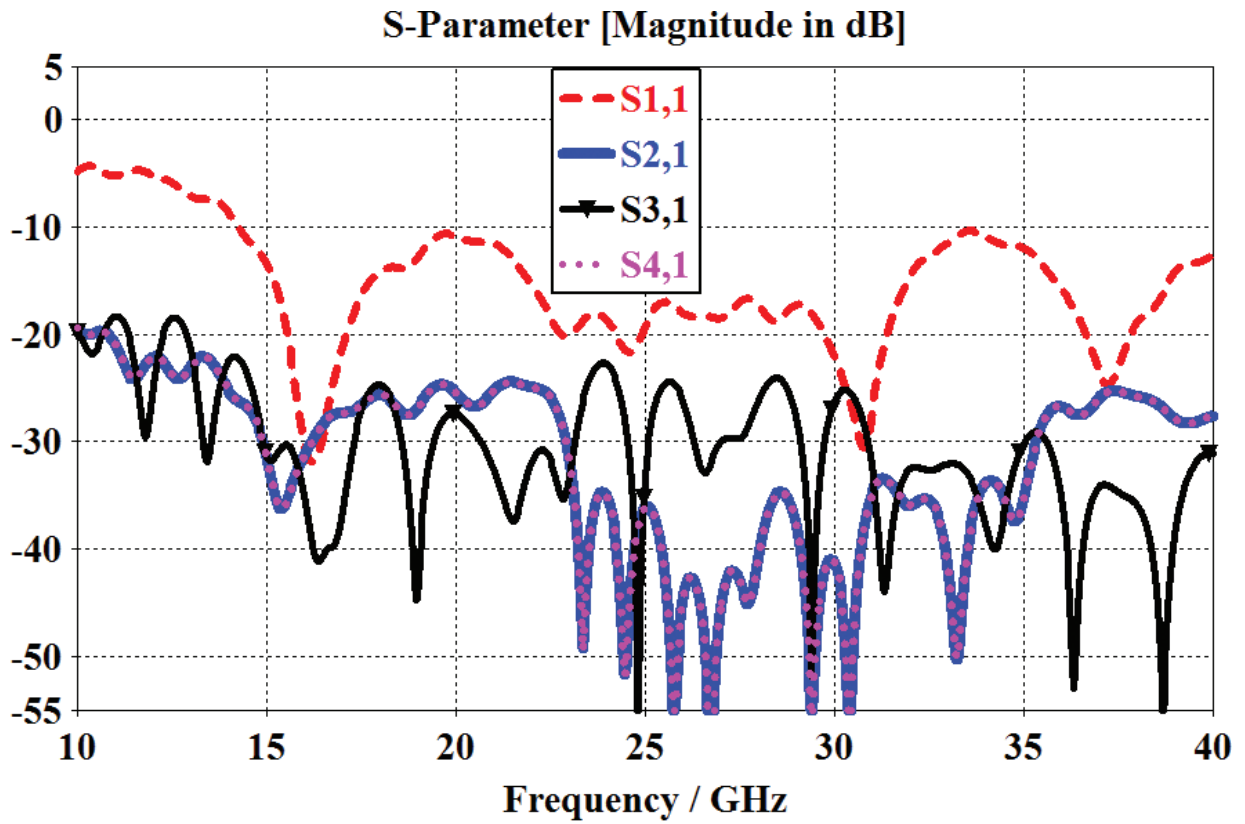


**Figure 12.** S-parameters of four-element beam-switched antenna system [38].

The four-element conformal ATSAs loaded with a dielectric lens are simulated to calculate and analyze S-parameters using the full-wave simulation program CST Microwave Studio [20]. The proposed conformal configuration of ATSAs does not affect the impedance bandwidth of the original design, since the mutual coupling between the antenna elements is



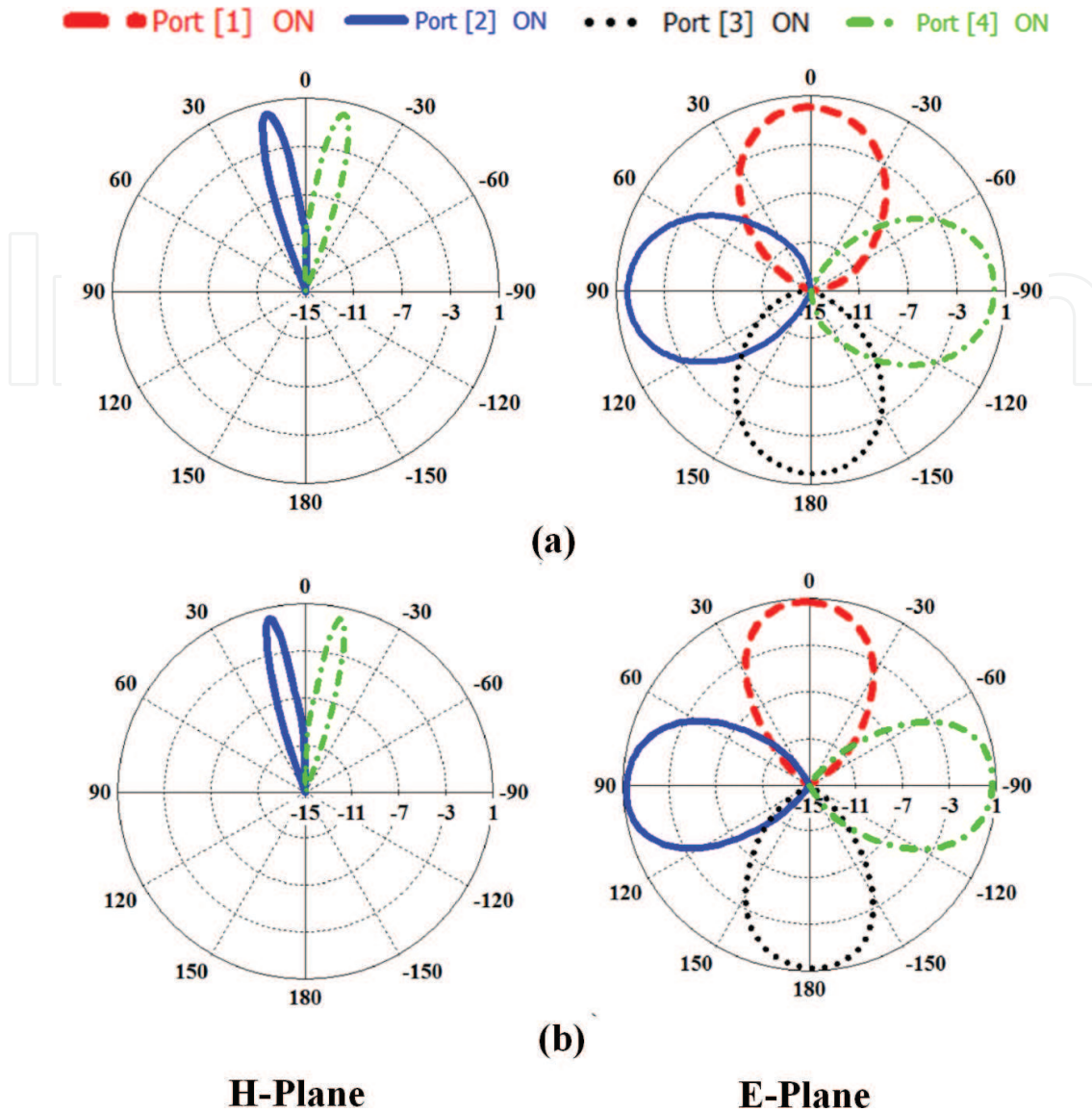


**Figure 13.** H-plane (antenna 2 and antenna 4) and E-plane (all antennas) switched beam radiation patterns at (a) 28 GHz and (b) 38 GHz. Beam switches at each co-ordinate axis ( $\pm x, y$ ) displaced by  $12^\circ$  in H-plane [38].

below  $-20$  dB over the complete spectrum, as shown in **Figure 12**. The minimum values of the reflection coefficient and mutual coupling values are below  $-10$  and  $-20$  dB, respectively, from 14.8 to 40 GHz. Moreover, better isolations are achieved between antenna elements 1 and 3. Considering the frequencies 28 and 38 GHz proposed for 5G wireless communications, the designed switched-beam ATSAs exhibit excellent S-parameter performance at those particular frequencies. Due to the symmetry of the designed configuration, only the S-parameter results for ATSA 1 are presented. The radiation performance of the proposed antenna configuration is calculated by exciting the particular element and terminating the other element with  $50\text{-}\Omega$  matched loads. Consider the proposed conformal configuration (see **Figure 11**) where antenna 1 and antenna 3 are placed opposite to each other at the  $-ve$  and  $+ve$   $x$ -axis, respectively. Similarly, antenna 1 and antenna 3 are placed at the  $-ve$  and  $+ve$   $y$ -axis, respectively. Since the dielectric lens is placed off-center with respect to each antenna element, exciting



antenna 1 enables the focusing of electromagnetic energy toward the +ve  $x$ -axis and vice versa. The same phenomenon is observed between antenna 2 and antenna 4. The calculated H-plane and E-plane radiation patterns with their respective excitations at different ports are shown in **Figure 13**. For the excitation of antenna 2 and antenna 4, the H-plane pattern is calculated by taking theta ( $\theta$ ) cut at the  $\varphi = 90^\circ$  plane. Antenna 2 and antenna 4 find beams switched at  $\theta = 12^\circ$  and  $\theta = -12^\circ$ , respectively. Similarly, the same radiation pattern results for antenna 1 and antenna 3 in the H-plane are observed at  $\varphi = 0^\circ$  cut. The E-plane radiation pattern is calculated by taking phi ( $\varphi$ ) cut at  $\theta = 12^\circ$ . It is worth noticing that the consecutive excitation of each individual port can result in four orthogonal switched beams placed  $90^\circ$  apart from each other.

## 6. 60-GHz radio or MMW antenna array for cloud computing

In this section, a simulated design of an MMW and array or 60-GHz radio band is presented for a cloud computing architecture. The design achieves the minimum requirements for the 60-GHz radio in terms of wide bandwidth (7 GHz at least, i.e., 57–64 GHz) and high gains ( $\sim 8$  dBi). The proposed antenna design is based on the aperture coupling technique [17, 38] that alleviates the problem of feedline and conductor losses while working at higher frequencies. The design consists of a multilayer structure with an aperture-coupled microstrip patch and a surface-mounted horn integrated on an FR4 substrate. The proposed antenna contributes an impedance bandwidth of 10.58% (58.9–65.25 GHz). The overall antenna gain and directivity are about 11.78 and 12.51 dBi, respectively. The antenna occupies an area of  $7.14 \text{ mm} \times 7.14 \text{ mm} \times 4 \text{ mm}$  with an estimated efficiency of 82%. In order to make the antenna more directive and to further increase the gain, a  $2 \times 2$  and  $4 \times 4$  array structure with a corporate feed network is introduced as well. The side lobe levels of the array designs are minimized, and the back radiations are reduced by utilizing a reflector at a  $\lambda/4$  distance from the corporate feed network. The  $2 \times 2$  array structure resulted in an improved gain of 15.3 dB with an efficiency of 83%, while the  $4 \times 4$  array structure provided further gain improvement of 18.07 dB with 68.3% efficiency. The proposed design is modeled in CST Microwave Studio, and its results are verified using HFSS.

### 6.1. Wideband and high-gain aperture-coupled microstrip patch antenna (ACMPA) with mounted horn for MMW communication

The geometry of the single-element multilayer ACMPA integrated with a mounted horn antenna on an FR4 substrate is shown in **Figure 14**. The 3D exploded view shows the entire multilayer structure with relevant parameters. For the first and second layers, RT/duroid<sup>®</sup> 5880 Laminate having dielectric constant  $\epsilon_r = 2.2$  and loss tangent 0.003 is used, while the third layer has an FR4 substrate with a dielectric constant of 4.3. A Rohacell foam is also placed on top of the FR4 substrate to assist the mounted horn antenna. The optimized dimensions of the horn antenna can be obtained from the guidelines listed in Ref. [40]. The conducting materials for the substrate have copper as an element with a thickness of  $t = 0.0175 \text{ mm}$ . The optimized dimensions of the proposed ACMPA are listed in **Table 5**.

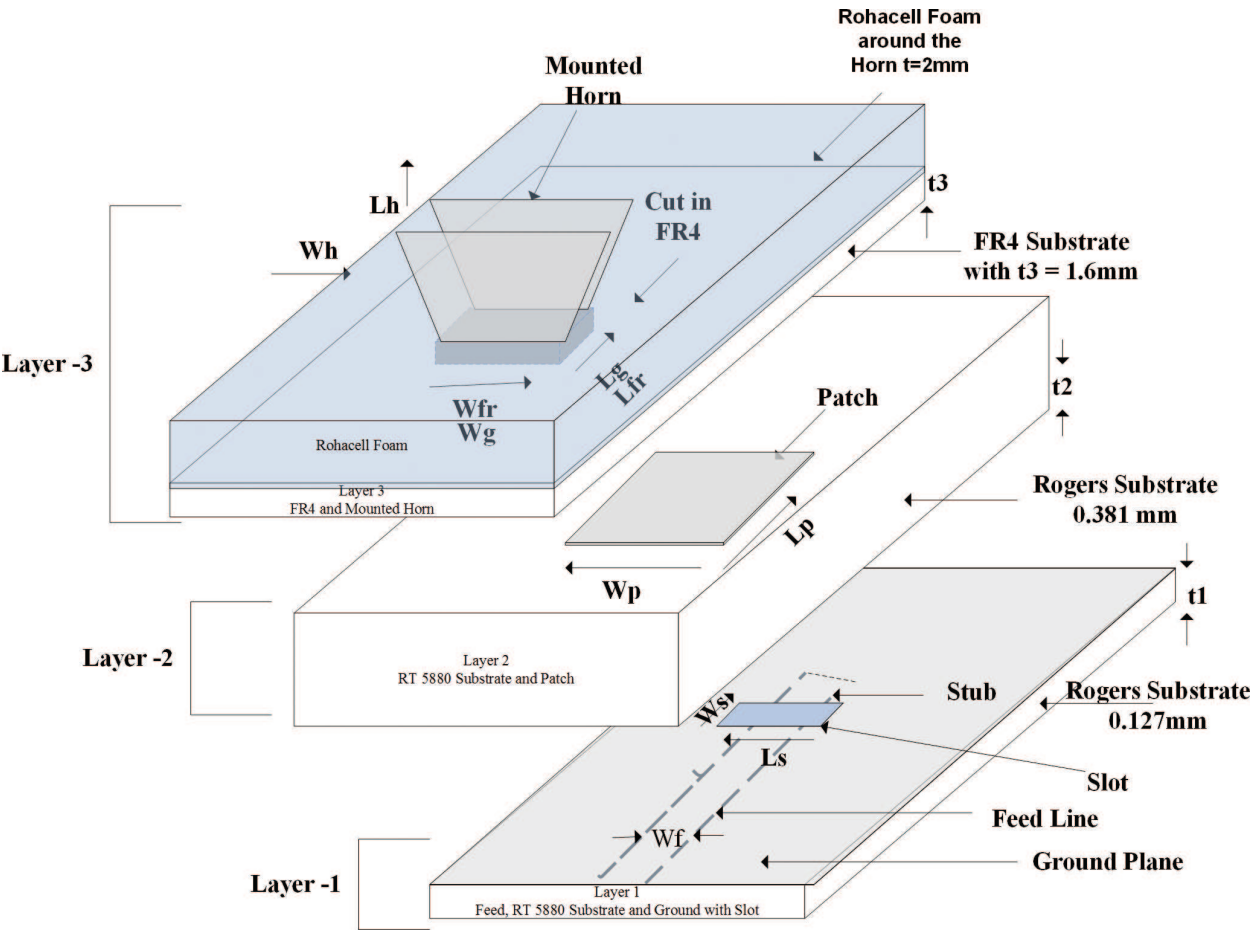


Figure 14. 3D exploded view of proposed ACMPA with relevant dimensions [39].

Design	Antenna element	Dimensions/parameters (mm)
Layer I	Microstrip feed	Feed width, $W_f = 0.386$
		Thickness, $t = 0.0175$
	Substrate	Stub length, $L_s = 0.45$
		RT Duroid 5880
		Length, $L = 30$
	Ground	Width, $W = 30$
		Thickness, $t_1 = 0.127$
Layer II	Rectangular slot	Length $L = 30$
		Width $W = 30$
	Substrate	Slot length, $L_s = 1$
		Slot width, $W_s = 0.2$
		RT Duroid 5880
		Thickness, $t_2 = 0.381$
		Length, $L = 30$

Design	Antenna element	Dimensions/parameters (mm)
Layer III	Patch	Width, $W = 30$
		Length, $L_p = 1.2$
		Width, $W_p = 1.2$
	Substrate	FR 4
	Cut in FR-4	Thickness, $t_3 = 1.6$
Horn	Horn dimensions	Length, $L_{fr} = 3$
		Width, $W_{fr} = 4.25$
		Horn length, $L_h = 7.14$
		Horn width, $W_h = 7.14$
		Waveguide length, $L_g = 3$
Full structure	Total height	Waveguide width, $W_g = 4.25$
		Thickness of metal horn, $t = 2$
		4

Table 5. Optimized dimensional parameters of the proposed ACMPA.

6.2. Results and discussion

Antenna design simulation tools were used to optimize and verify the proposed ACMPA design. The return loss S11 parameters below the -10 dB resonance and the gain of the antenna are shown in **Figure 15**. The antenna achieves an impedance of 10.58% (58.9–65.25 GHz) with a gain and efficiency of 11.78 dB and 88%, respectively. Substrate and metallic losses were taken into account during simulations. **Figure 16(a)** and **(b)** show the E-plane and H-plane radiation patterns, simulated in CST and HFSS, of the proposed antenna, for the frequencies at 59, 62, and 65 GHz, respectively. Thus, for the multilayer structure at 62 GHz, the E-plane has a side lobe of level -5 dB, half-power beamwidth of 31°, and back radiation of -18.3 dB. The H-plane radiation pattern at 62 GHz has a side lobe of -13.2, half-power beamwidth of 69.8°, back radiation of -17dB, and cross-polarization level of >-30 dB.

6.3. 2 × 2 and 4 × 4 ACMPA array design

MMWs or 60-GHz radio bands offer wide bandwidth and higher gains for short-range communications. In order to fulfill these requirements, especially that of higher gain, the proposed ACMPA was optimized in terms of arrays (i.e., 2 × 2 and 4 × 4). Two factors are important when designing arrays: (1) array factor and (2) feeding network impedances. The theory behind the antenna array factor was utilized as explained in Ref. [41], where each antenna element is treated as an individual isotropic point source. Energy contributions from each point source are derived in the far field expressed as array factor (AF). For the feed network, one can select either single feed or parallel/corporate feed depending on the design requirements. For our proposed design, since we are working at higher (i.e., 60 GHz) bands, we opted for the corpo-

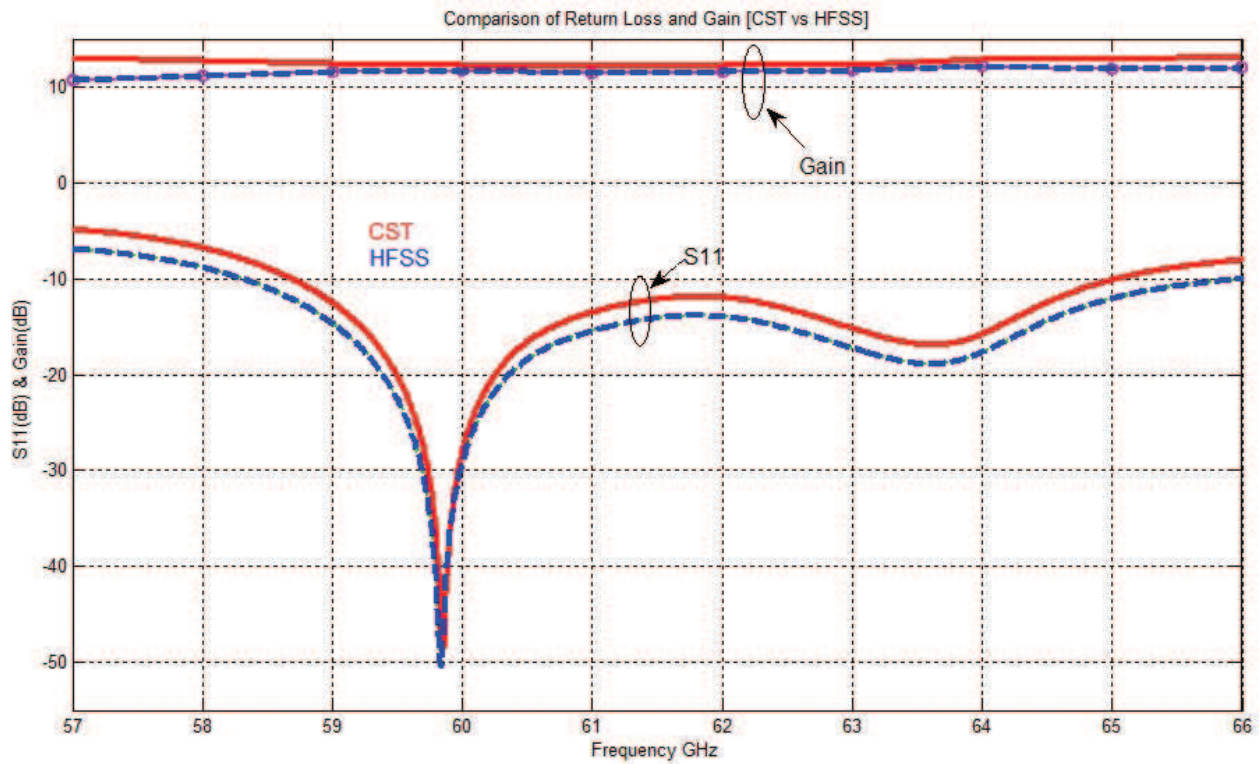


Figure 15. S-parameters and gain of proposed ACMPA.

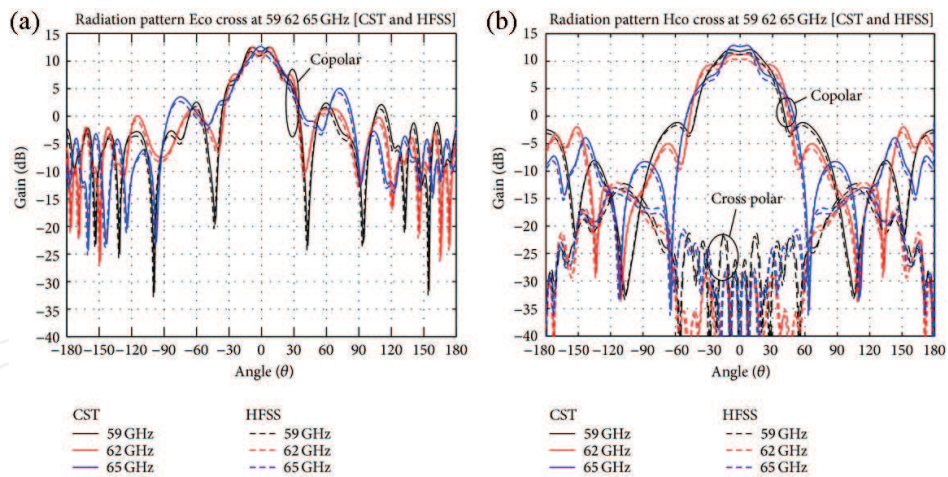


Figure 16. (a) Simulated E-plane radiation pattern at 59, 62, and 65 GHz and (b) simulated H-plane radiation pattern at 59, 62, and 65 GHz [39].

rate feed network, as it would suppress further losses encountered during analysis. A general  $2 \times 2$  and  $4 \times 4$  corporate feed network is shown in **Figure 17(a)** and **(b)** with relevant impedances. Corporate feed networks are in general very versatile, as they offer power splits of  $2n$  (i.e.,  $n = 2, 4, 8, 16, 32$ , etc.) and control to the designer in terms of amplitude and phase selection of the individual feed element and its power division among the transmission lines. It is ideal for scanning phased arrays, shaped-beam arrays, and multibeam arrays [41]. The length and



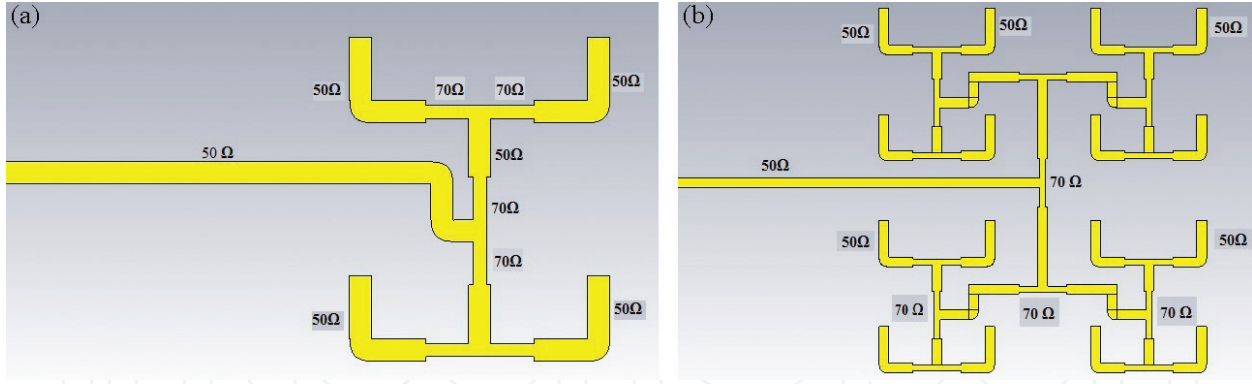


Figure 17. Corporate feed network (a)  $2 \times 2$  array and (b)  $4 \times 4$  array.

width of the transmission lines can be varied as per the requirement of the power division. The feed network consists of a  $50\text{-}\Omega$  transmission line and a  $70.7\text{-}\Omega$  quarter-wavelength transformer matched to a primary  $50\text{-}\Omega$  feeding line. For the  $2 \times 2$  and  $4 \times 4$  arrays with reflectors, the corporate feed network's impedance values can be retrieved from the guidelines provided in Ref. [42–44]. Figure 18(a) and (b) show the exploded view of the proposed array designs.

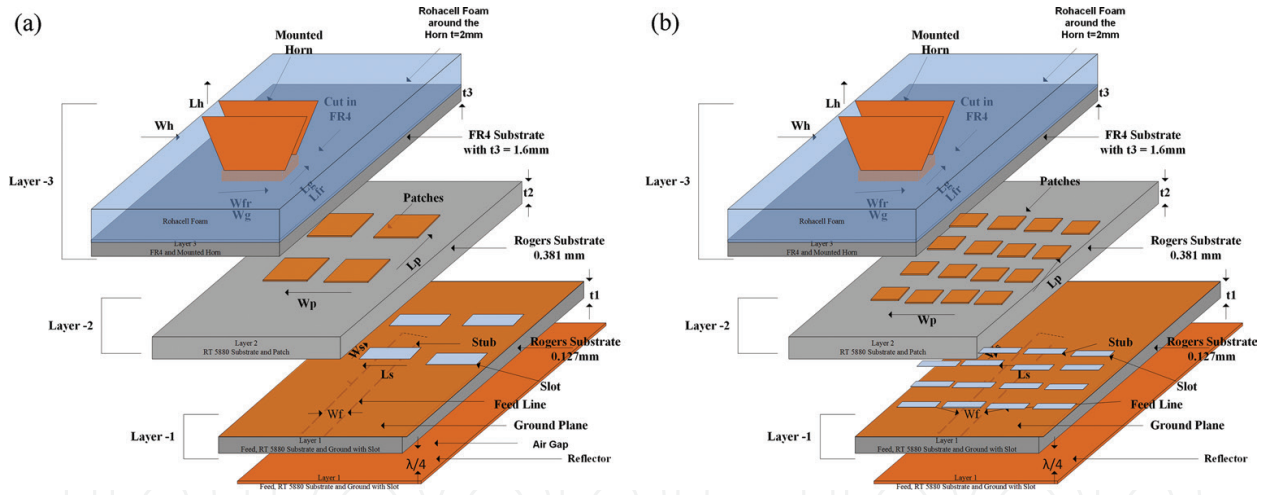
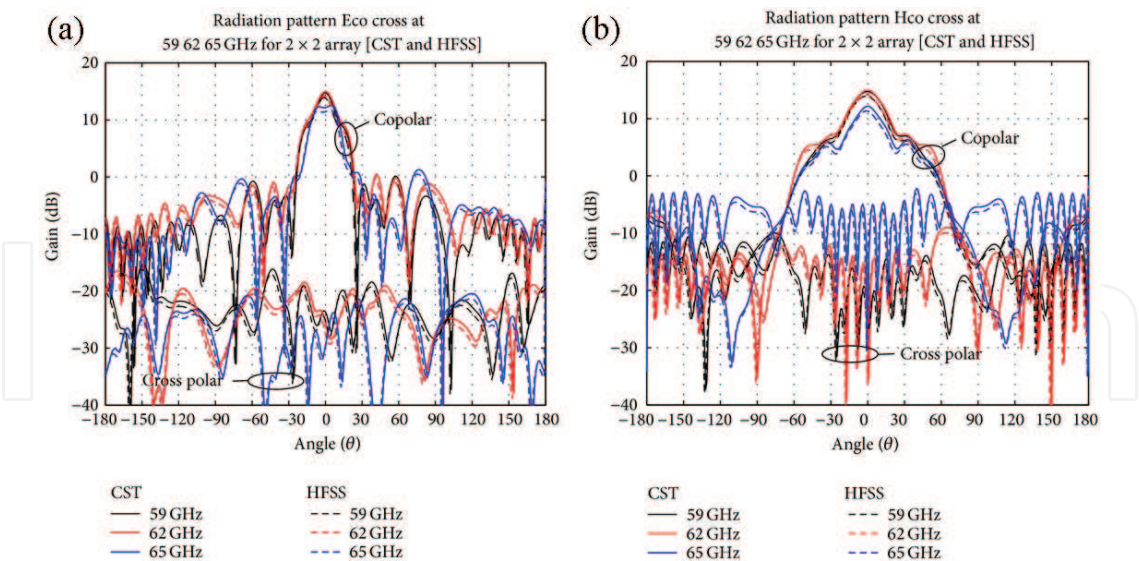


Figure 18. Exploded view (a)  $2 \times 2$  array and (b)  $4 \times 4$  array [39].

The E-plane and H-plane radiation patterns for the  $2 \times 2$  array and  $4 \times 4$  arrays are shown in Figures 19 and 20. For the  $2 \times 2$  array, it is observed that the E-plane at 62 GHz has a side lobe of level  $-13.7\text{ dB}$ , half-power beamwidth of  $22.1^\circ$ , and back radiation of  $-25.3\text{ dB}$ . The H-plane radiation pattern at 62 GHz has a side lobe of  $-9.1\text{ dB}$ , half-power beamwidth of  $22.2^\circ$ , back radiation of  $-21.8\text{ dB}$ , and cross-polarization level of  $>-30\text{ dB}$ . For the  $4 \times 4$  array, the E-plane at 62 GHz has a side lobe of level  $-11.8\text{ dB}$ , half-power beamwidth of  $13.6^\circ$ , and back radiation of  $-23.07\text{ dB}$ . The H-plane radiation pattern at 62 GHz has a side lobe of  $-12.4$ , half-power beamwidth of  $16.1^\circ$ , and back radiation of  $-23.07\text{ dB}$ . Table 6 shows the comparison of the improved gain from a single element to  $2 \times 2$  and  $4 \times 4$  arrays.





**Figure 19.** (a) Simulated E-plane radiation pattern at 59, 62, and 65 GHz and (b) simulated H-plane radiation pattern at 59, 62, and 65 GHz [39].

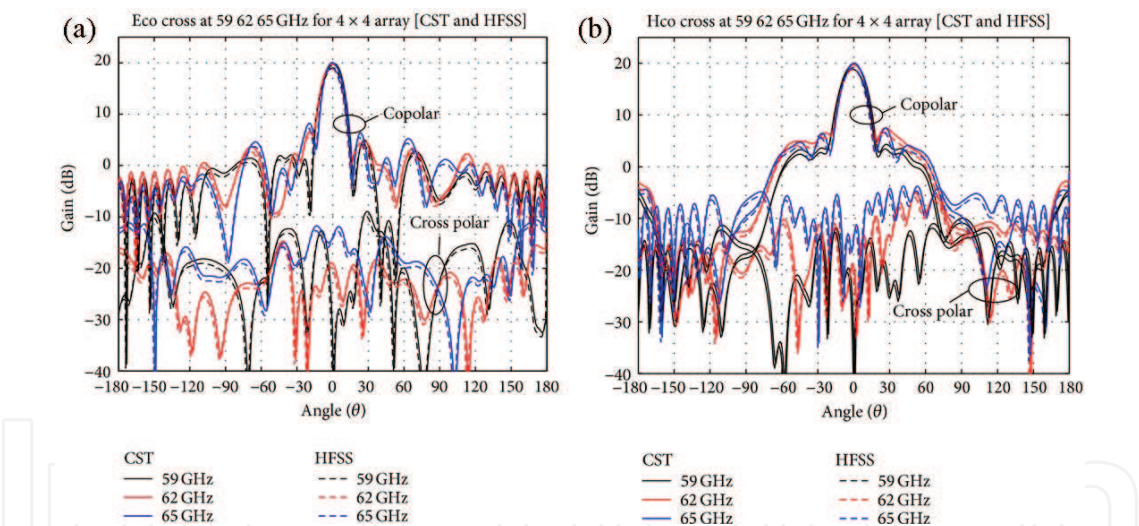


**Figure 20.** (a) Simulated E-plane radiation pattern at 59, 62, and 65 GHz and (b) simulated H-plane radiation pattern at 59, 62, and 65 GHz [39].

Array/parameters	Single element	$2 \times 2$ array	$4 \times 4$ array
Bandwidth (%)	10.58	10.55	10.51
Gain (dB)	11.78	15.3	18.07
Efficiency (%)	88	83	68.3

**Table 6.** Simulated results of single element,  $2 \times 2$  and  $4 \times 4$  array.

## Acknowledgements

This research is supported by King Abdul Aziz City for Science and Technology and Lockheed Martin (KACST-LM) University funding program.

## Author details

Waleed Tariq Sethi<sup>1</sup>, Abdullah Alfakhri<sup>2</sup>, Muhammad Ahmad Ashraf<sup>1\*</sup>, Amr G. Alasaad<sup>2</sup> and Saleh Alshebeili<sup>1</sup>

\*Address all correspondence to: mashraf@ksu.edu.sa

1 KACST Technology Innovation Center in Radio Frequency and Photonics for the e-Society (RFTONICS), King Saud University, Riyadh, Saudi Arabia

2 Center of Excellence in Future Telecommunication Applications, KACST, Riyadh, Saudi Arabia

## References

- [1] Cisco Visual Networking Index, Global mobile data traffic forecast update, 2015–2020, White Paper, updated Feb 01, 2016.
- [2] A. Checko, H. L. Christiansen, Y. Yan, L. Scolari, G. Kardaras, M. S. Berger, and L. Dittmann, "Cloud RAN for mobile networks—a technology overview," in *IEEE Communications Surveys & Tutorials*, vol. 7, no. 1, 2015.
- [3] A. Arbi and T. O'Farrell, "Energy efficiency in 5G access networks: small cell densification and high order sectorisation," in *Proc. of the IEEE International Workshop on Communication*, pp. 2806–2811, 2015.
- [4] Y. Cai, F. R. Yu, and S. Bu, "Cloud radio access networks (C-RAN) in mobile cloud computing systems," in *Proc. of the IEEE Infocom Workshops*, pp. 369–374, 2014.
- [5] A. K. Sultanov, et al., "IR-UWB radio-over-fiber system components development," *XIII International Scientific and Technical Conference on Optical Technologies in Telecommunications*, International Society for Optics and Photonics, 2016.
- [6] Federal Communications Commission, "FCC report and order for part 15 acceptance of ultra wideband (UWB) systems from 3.1–10.6 GHz," FCC, Washington, DC, 2002.
- [7] A. M. Abdelraheem, and M. A. Abdalla. "Compact curved half circular disc-monopole UWB antenna," *International Journal of Microwave and Wireless Technologies*, 8 02 (2016), 283–290.
- [8] D. Upadhyay, I. Acharya, and R. P. Dwivedi, "A novel circular monopole fractal antenna for bluetooth and UWB applications with subsequent increase in gain using frequency

selective surfaces," *Information Systems Design and Intelligent Applications*, Springer India, 2016, 337–348.

- [9] Z. N. Chen, et al., "Planar antennas," *Microwave Magazine, IEEE*, vol. 7, pp. 63–73, 2006.
- [10] S. H. Choi, et al., "A new ultra wideband antenna for UWB applications," *Microwave and Optical Technology Letters*, vol. 40, pp. 399–401, 2004.
- [11] S. H. Choi, et al., "Clover-shaped antenna for ultra-wideband communications," *Microwave and Optical Technology Letters*, vol. 48, pp. 2111–2113, 2006.
- [12] J. Liang, et al., "Printed circular disc monopole antenna for ultra-wideband applications," *Electronics Letters*, vol. 40, pp. 1246–1247, 2004.
- [13] C. Ying and Y. Zhang, "Integration of ultra-wideband slot antenna on LTCC substrate," *Electronics Letters*, vol. 40, pp. 645–646, 2004.
- [14] J. N. Lee and J. K. Park, "Impedance characteristics of trapezoidal ultra-wideband antennas with a notch function," *Microwave and Optical Technology Letters*, vol. 46, pp. 503–506, 2005.
- [15] A. Boryssenko and D. Schaubert, "Physical aspects of mutual coupling in finite broadband tapered slot (Vivaldi) arrays," in *5th International Conference on Antenna Theory and Techniques*, 2005, 2005, pp. 74–79.
- [16] M. Kyro; V. Kolmonen; P. Vainikainen; D. Titz; C. Villeneuve, "60 GHz membrane antenna array for beam steering applications," *6th European Conference on Antennas and Propagation (EUCAP)*, 26–30 March 2012, 2012, pp.2770–2774.
- [17] J. Bai, S. Shi, D. W. Prather, "Modified compact antipodal Vivaldi antenna for 4–50-GHz UWB application," *IEEE Transactions on Microwave Theory and Techniques*, vol.59, no.4, pp.1051–1057, April 2011.
- [18] J. Grzyb; D. Liu, U. Pfeiffer, B. Gaucher, "Wideband cavity-backed folded dipole superstrate antenna for 60 GHz applications," *Antennas and Propagation Society International Symposium 2006, IEEE*, vol., no., pp. 3939–3942, 9–14 July 2006.
- [19] Y. Li, Z. Ning Chen, X. Qing, Z. Zhang, J. Xu; Z. Feng, "Axial ratio bandwidth enhancement of 60-GHz substrate integrated waveguide-fed circularly polarized LTCC antenna array," *IEEE Transactions on Antennas and Propagation*, vol. 60, no.10, pp. 4619–4626, Oct. 2012.
- [20] H. Vettikalladi, O. Lafond and M. Himdi, "Superstrate antennas for wide bandwidth and high efficiency for 60 GHz indoor communications," *Institute of Electronics and Telecommunication of Rennes (IETR)*, University of Rennes 1, InTech, France, 2012.
- [21] S. Ononchimeg, G. Otgonbaatar, J.-H. Bang, and B.-C. Ahn, "A new dual polarized horn antenna excited by a gap-fed square patch," *Progress in Electromagnetics Research Letters*, 129–137, vol 21, 2011.
- [22] K. Hettak, G. Y. Delisle, G. A. Morin, S. Toutain and M. Stubbs, "A novel variant 60-GHz CPW-fed patch antenna for broadband short range wireless communications," *Antennas and Propagation Society International Symposium*, 1–4, 2008.

- [23] H. Vettikalladi; L Le Coq; O Lafond and M. Himdi, "Wideband and high efficient aperture antenna with superstrate for 60 GHz indoor communication systems," *2010 IEEE AP-S International Symposium on Antennas and Propagation and 2010 USNC/CNC/URSI Meeting in Toronto, ON, Canada, on July 11–17, 2010*, 2010.
- [24] M. B. Gueye, H. H. Ouslimani S. N. Burkour, A. Priou, "Antenna array for point-to-point communication in E-band frequency range," *AP-S/URSI*, 2011.
- [25] A. Elboushi and A. Sebak, "High-gain hybrid microstrip/conical horn antenna for MMW applications," *IEEE Transactions on Antennas and Propagation*, vol. 61 no. 11, 2012.
- [26] N. Caille, S. Pine, C. Quendo, C. Person, E. Rius, J- F. Favennec and J. Laskar, "Foam micromachined aperture-coupled antennas for V-band low-cost applications," *Proceedings of the 37th European Microwave Conference*.
- [27] O. Kramer, T. Djerfi, and K. Wu, "Very small footprint 60 GHz stacked yagi antenna array," *IEEE Transactions on Antenna and Propagation*, vol. 59 no. 9, September 2011.
- [28] H. Vettikalladi, L. Le Coq, O. Lafond, M. Himdi, "Efficient and high-gain aperture coupled superstrate antenna arrays for 60 GHz indoor communication systems," *Microwave and Optical Technology Letters*, Vol 52, No. 10, Oct. 2010.
- [29] P. A. Hoeher, and N. Doose, "A massive MIMO terminal concept based on small-size multi-mode antennas," *Transactions on Emerging Telecommunications Technologies*, (2015).
- [30] R. Ma; Y. Gao; L. Cuthbert; Q. Zeng, "Antipodal linearly tapered slot antenna array for millimeter-wave base station in massive MIMO systems," *Antennas and Propagation Society International Symposium (APSURSI), 2014 IEEE*, vol., no., pp. 1121–1122, 6–11 July 2014.
- [31] C.-H. Tseng; C.-J. Chen; T.-H. Chu, "A low-cost 60-GHz switched-beam patch antenna array with Butler matrix network," *IEEE Antennas and Wireless Propagation Letters*, vol.7, no., pp. 432–435, 2008.
- [32] W. F. Moulder; W. Khalil; J. L. Volakis, "60-GHz two-dimensionally scanning array employing wideband planar switched beam network," *IEEE Antennas and Wireless Propagation Letters*, vol. 9, no., pp. 818–821, 2010.
- [33] V. Semkin; F. Ferrero; A. Bisognin; J. Ala-Laurinaho; C. Luxey; F. Devillers; A. V. Raisanen, "Beam switching conformal antenna array for mm-wave communications," *IEEE Antennas and Wireless Propagation Letters* , vol. 99, pp. 1–1, 2015.
- [34] M. A. Ashraf, et al., "Modified antipodal Vivaldi antenna with shaped elliptical corrugation for 1–18-GHz UWB application," *Applied Computational Electromagnetics Society Journal*, 30 1 (2015), 68–77.
- [35] J. Y. Siddiqui; Y. M. M. Antar; A. P. Freundorfer; E. C. Smith; G. A. Morin; T. Thayaparan, "Design of an ultrawideband antipodal tapered slot antenna using elliptical strip conductors," *IEEE Antennas and Wireless Propagation Letters* , vol. 10, pp. 251–254, 2011.



- [36] Studio, CST Microwave. "3D EM Simulation software." *Computer Simulation Technology* (2014).
- [37] D.-H. Kwon, "Effect of antenna gain and group delay variations on pulse-preserving capabilities of ultrawideband antennas," *IEEE Transactions on Antennas and Propagation*, vol. 54, no. 8, pp. 2208–2215, Aug. 2006.
- [38] M. A. Ashraf; O. M. Haraz; and S. Alshebeili, "Compact size enhanced gain switched beam conformal antipodal tapered slot antenna system for 5G MIMO wireless communication," *IEEE 11th International Conference on Wireless and Mobile Computing, Networking and Communications (WiMob)*, 2015, Abu Dhabi, 2015, pp. 613–618.
- [39] H. Vettikalladi; W. T. Sethi; and M. A. Alkanhal, "High gain and high efficient stacked antenna array with integrated horn for 60 GHz communication systems," *International Journal of Antennas and Propagation*, vol. 2014, Article ID 418056, 8 pages, 2014. doi:10.1155/2014/418056
- [40] P. Kumar; D. Batra; and A. K. Shrivastav, "High gain microstrip antenna capacitive coupled to a square ring with surface mounted conical horn," *Journal of Communications Technology and Electronics*, vol. 1, no. 1, pp. 7–9, 2010.
- [41] H. Vettikalladi; O. Lafond; and M. Himdi; "High-efficient and high-gain superstrate antenna for 60-GHz indoor communication," *IEEE Antennas and Wireless Propagation Letters*, vol. 8, pp. 1422–1425, 2009.
- [42] W. T. Sethi; H. Vettikalladi; and M. A. Alkanhal; "Millimeter wave antenna with mounted horn integrated on FR4 for 60 GHz Gbps communication systems," *International Journal of Antennas and Propagation*, vol. 2013, Article ID 834314, 5 pages, 2013. doi:10.1155/2013/834314
- [43] C.A. Balanis, "Antenna theory: analysis and design," 2nd ed. New York John Wiley and Sons, Inc., (1997).
- [44] W. T. Sethi; H. Vettikalladi; and M. A. Alkanhal, "High gain stacked antenna array for 60 GHz communication systems," 2014 *IEEE Antennas and Propagation Society International Symposium (APSURSI)*, Memphis, TN, 2014, pp. 1734–1735. doi: 10.1109/APS.2014.6905193



